ACS Catalysis

Research Article

pubs.acs.org/acscatalysis

Polymer-Assisted Hydrothermal Synthesis of Highly Reducible Shuttle-Shaped CeO_2: Microstructural Effect on Promoting Pt/C for Methanol Electrooxidation

Sumanta Kumar Meher and G. Ranga Rao*

Department of Chemistry, Indian Institute of Technology Madras, Chennai 600036, India

ABSTRACT: Here, a simple polymer (P123)-assisted homogeneous precipitation method has been employed to synthesize unique shuttle-shaped CeO_2 in gram scale. The physicochemical properties, such as crystallographic identity, surface area, and pore characteristics of the shuttle-shaped CeO_2, are found to be significantly better as compared with bulk CeO_2 synthesized under a polymer-free medium. The H_2-TPR study shows very low temperature (~268 °C) surface reduction, which demonstrates the presence of a larger size and number of oxygen vacancy clusters as well as more reactive surface oxygen species on the shuttle-shaped CeO_2. The microstructural affect of CeO_2 on the nature of Pt dispersion has been investigated by HRTEM, which shows that because of a higher number of surface defect sites, nanostructured shuttle-shaped CeO_2 induces better Pt−CeO_2 interaction and miniaturization as well as effective dispersion of Pt nanocrystallites in the composite. Further, the microstructural effect of CeO_2 in promoting Pt/C for methanol electrooxidation reaction in acidic medium has been studied using various electrochemical techniques. The cyclic voltammetry and CO stripping voltammetery studies show that the nanostructured shuttle-shaped CeO_2 highly promotes methanol electrooxidation reaction (higher oxidation current and lower oxidation overpotential) as compared with the bulk CeO_2. This is due to a higher number of triple-phase interfacial active centers on the shuttle-shaped CeO_2 surface, which provide additional OH_{ads} species for oxidation of poisoning carbonaceous species at lower overpotential. The activity studies using chronopotentiometry and chronoamperometry techniques show that unlike bulk CeO_2, nanostructured shuttle-shaped CeO_2 provides significant antipoisoning activity to Pt/C during the methanol electrooxidation reaction. This study, for the first time, provides evidence that CeO_2 with a suitable microstructure can improve the electrocatalytic activity of Pt/C for methanol oxidation, and this approach can be exploited for designing other electrocatalysts for fuel cell applications.

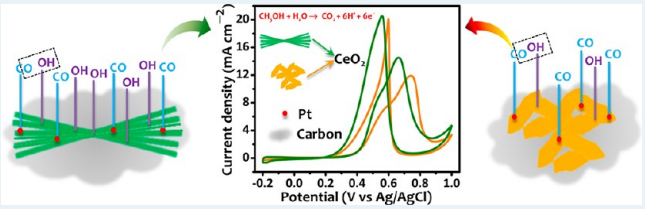

KEYWORDS: *shuttle-shaped CeO_2, reducibility, oxide promoter, methanol electrooxidation, electrocatalysis*

1. INTRODUCTION

Among the array of efficient, renewable and environmentally friendly energy storage systems, fuel cells have emerged as one of the most versatile devices in which energy is produced in the form of electrical energy via redox reaction-mediated electrochemical conversion of chemical energy.[1−3] Fuel cells have been categorized on the basis of either the electrolyte employed or the operating temperature of the cell. For instance, alkaline fuel cells, polymer electrolyte fuel cells, direct methanol fuel cells (DMFC) and phosphoric acid fuel cells are low-temperature fuel cells, whereas molten carbonate fuel cells and the solid oxide fuel cells are categorized as high-temperature fuel cells. Among these, DMFC, in particular, because of its higher energy density, use of liquid fuel (methanol), low operating cost, and compact design, shows great promise for practical application in transport and portable device applications.[4−7] The operating principle of DMFC is rather simple and involves the following electrochemical steps:

$$\text{anode:} \quad CH_3OH(l) + H_2O(aq) \rightarrow CO_2(g) + 6H^+ + 6e^-$$

$$\text{cathode:} \quad \frac{3}{2}O_2(g) + 6H^+ + 6e^- \rightarrow 3H_2O(l)$$

$$\text{overall reaction:} \quad CH_3OH(l) + \frac{3}{2}O_2(g) \rightarrow CO_2(g) + 2H_2O(l)$$

Pt is found to be the most active electrocatalyst in order to achieve faster kinetics of the anodic reaction during electrooxidation of methanol.[8] Pt is a precious metal and is therefore highly expensive, and hence, activated carbon is mostly used as a support for the stability, dispersion, and improved utilization of Pt. However, because of extremely weak van der Waals interaction between Pt and carbon, rapid agglomeration (via Ostwald ripening) as well as detachment of Pt occurs during device operation.[9] Furthermore, during the anodic process, carbonaceous species such as CO are produced as reaction intermediates during the breakdown of methanol, which heavily poison the Pt surface and inhibit further adsorption of methanol molecules, lowering the methanol electrooxidation kinetics.[10] Hence, the performance of Pt-based catalysts worsens with time, and long-term usage of the device becomes hypothetical.[11]

To avoid the poisoning of Pt catalysts, the most exploited strategy has been the alloying of Pt with additional metals, such as Ru, Rh, Sn, Ir, Os, Re, Mo, V, Cr, Co, Ni, Cu, etc., in binary ternary and quaternary fashion.[12,13] In principle, the additional

Received: July 16, 2012
Revised: September 29, 2012
Published: November 6, 2012

   dx.doi.org/10.1021/cs300473e | ACS Catal. 2012, 2, 2795−2809

metals, because of their oxophilicity, are prone to adsorption of oxygenated species such as OH at lower potential, and hence, their presence promotes oxidation of CO to CO_2 via the well-known bifunctional mechanism as well as electronic effect.[14,15] However, most of the additional metals in the Pt-based alloys are also noble and commercially nonfeasible. In view of the fact that size, structure, shape, and active surface area are very important for preferential adsorption of methanol, the shape-selective nanostructurization of the electrocatalysts is rather essential;[16,17] however, uniform nanostructurization of homogeneous multicomponent metallic catalysts is quite tedious, and their synthesis in large scale for commercial utilization is impractical. The multicomponent metallic electrocatalysts are also prone to segregation during device operation.[11]

In recent years, metal oxides that allow activation of water at lower potentials and can efficiently undergo a bifunctional mechanism have shown immense promise for promoting electrocatalytic and antipoisoning activity of Pt.[18,19] In this context, various metal oxides, such as RuO_2, WO_3, ZrO_2, MgO, MoO_2, MoO_3, TiO_2, V_2O_5, Nb_2O_5, and CeO_2 in combination with carbon have been exploited for optimized dispersion of Pt and electrooxidation of methanol.[18−28] These composites are reported as highly promising electrocatalysts and show significant tolerance to CO poisoning.

Among the range of low-cost oxides, CeO_2 is of particular interest as a result of its high surface area, sizable surface defects, and higher oxygen storage capacity (redox Ce^{4+}/Ce^{3+} sites).[29] Because of these incredible physicochemical properties, CeO_2 efficiently stabilizes dispersion of Pt, which favors increased active surface per weight of Pt and makes sufficient OH_{ads} species available at lower overpotential to oxidize majority of adsorbed poisoning species (like CO) on Pt, during methanol electrooxidation. In this context, a sizable number of reports showing excellent promotional and antipoisoning activities of CeO_2 for methanol electrooxidation are available in the literature.[28,30−37] However, most of the reports are purely based on the nanostructure effect of Pt, nature of Pt dispersion and Pt−CeO_2 interactions. It is known that the characteristic surface morphology/microstructure of CeO_2 manipulates the crystallographic orientation, exposed crystal surface, and size as well as the shape of the nanocrystals, which strongly influence the surface atom densities, electronic structure, and chemical reactivity.[38] Further, the surface reducibility of CeO_2 is greatly affected by its surface area and surface morphology/microstructure.[38,39]

In this context, a designed surface morphology/microstructure of CeO_2 with uniform crystalline orientation and smaller crystallite size is expected to achieve more active sites and good interfacial contact with Pt, which can strengthen interaction between Pt and CeO_2, inhibiting random growth as well as sintering of Pt particles for optimized synergic effect and methanol oxidation activity.[40] Further, a designed surface morphology/microstructure of CeO_2 with high reducibility is especially important for improved interaction with Pt, which in essence can improve the activity and durability of the catalysts.[41,42] However, in the available literature, the microstructural effect of CeO_2 on the dispersion of Pt and activity toward methanol electrooxidation is overlooked. Hence, it is of utmost importance to investigate the affect of the microstructural design of CeO_2 (size, shape, and surface properties) on the bonding and stability of Pt for the methanol electrooxidation reaction.

Recently, extensive efforts have been put forward to develop shape-controlled synthesis of various surface morphologies of CeO_2, such as nanotubes, 2D nanosheets, nanoplates, nanorods, and nanoflowers.[38,43] The growth of CeO_2 with faceted geometries is found to be greatly regulated by different solvents, anions, and surfactants in the reaction medium, which selectively adsorb on certain crystal planes and modulate the surface free energies, thereby kinetically controlling the growth of certain crystal planes to generate a specific surface morphology.[38,43] However, simple and classical methods for scalable synthesis of nanostructured CeO_2 with controlled surface morphology/microstructure, high surface area, optimal particle dimension/architecture, and suitably aligned nanocrystalline phases is still a key challenge.

In this context, this work deals with the synthesis of nanostructured CeO_2 with controlled surface morphology/microstructure using a polymer-assisted homogeneous precipitation method under hydrothermal conditions. Here, we have studied the microstructural affect of CeO_2 on the nature of the Pt−CeO_2 interaction and antipoisoning as well as catalytic promoting activities of CeO_2 to Pt/C for the methanol electrooxidation reaction.

2. EXPERIMENTAL SECTION

2.1. Synthesis of Nanostructured CeO_2. Analytical grade $Ce(NO_3)_3{\cdot}6H_2O$ (99.9%, SD Fine, India), poly(ethylene glycol)−poly(propylene glycol)−poly(ethylene glycol) (P123, Sigma-Aldrich) with a molecular weight of 5800 g, and urea (99.9%, Thomas-Baker) were used without further purification. Laboratory-prepared triple-distilled water was used during all the experimental processes. In a typical polymer-assisted synthesis of CeO_2, 20 mmol of $Ce(NO_3)_3.6H_2O$ was dissolved in 100 mL of triple-distilled water, and the resulting solution was added dropwise to 1 mmol of P123 dissolved in 100 mL triple-distilled water. The solution was stirred for 1 h to form a homogeneous solution. To the resulting solution, 80 mmol of solid urea was added, and the solution was stirred again for 3 h. The solution was then transferred to a stainless steel autoclave with an inside Teflon liner of 250 mL capacity and subjected to heating at 120 °C for 24 h. The autoclave was then allowed to cool to room temperature, and after aging the resultant product for 24 h, a white precipitate was separated by centrifugation at 3000 rpm. The white precipitate was then repeatedly washed with triple-distilled water followed by a mixture of absolute ethanol and water and, finally, with absolute ethanol several times. The resultant precipitate was then dried under vacuum at 60 °C for 24 h. To get the final product, the dried precursor sample was then subjected to thermal treatment at a rate of 10 °C min^{-1} from room temperature to 400 °C and heated at 400 °C for 3 h in flowing air. In a polymer-free synthesis of CeO_2, a procedure similar to that described above was followed, but in the absence of P123 in the reaction medium. The hydrothermal syntheses of the precursor samples via polymer-free and polymer-assisted procedures are denoted, respectively, as CeO_2-H-uc and CeO_2-HP-uc. The corresponding samples obtained after thermal treatment of CeO_2-H-uc and CeO_2-HP-uc precursors are denoted as CeO_2-H and CeO_2-HP.

2.2. Preparation of Electrocatalyst Composites. The Pt/C, Pt/CeO_2-H/C, and Pt/CeO_2-HP/C electrocatalysts were prepared by a microwave-assisted polyol process. The CeO_2 content in the different electrocatalysts was fixed at 20 wt %. For the preparation of a typical Pt/CeO_2-C catalyst, 20 mg of CeO_2 and 100 mg of Vulcan XC-72 carbon black

(Cabot Corporation, BET surface area of ~250 m^2 g^{-1}) were dispersed thoroughly in 100 mL of ethylene glycol (EG)−isopropyl alcohol (IPA) mixture (V/V = 4:1, AR grade) via ultrasonication for 30 min. A 1.282 mL portion of 0.1 M H_2PtCl_6 (Aldrich, ACS Reagent)−EG solution was then added to the above mixture, and the mixture was then sonicated for 15 min, followed by constant stirring for 6 h. The pH of the stirring mixture ink was adjusted to ~10 by dropwise addition of 1 M KOH−EG solution. Further, the mixture ink was treated with microwave radiation in a domestic microwave oven (Sharp NN-S327 WF, 2450 MHz, and 1100W) for 50 s for complete reduction of H_2PtCl_6 to Pt. The resulting product was then allowed to cool to room temperature with continuous stirring. The pH of the microwave-treated ink mixture was then adjusted to ~4 using 0.1 M HNO_3 solution and was further stirred for 12 h before filtering out the residue. The resultant product was then repeatedly washed with Millipore water, followed by acetone (AR grade), until it became free of the Cl^- ion. The product was then dried overnight under vacuum at 60 °C. The Pt/C electrocatalyst was prepared using a procedure similar to that described above, but without CeO_2. The amount of Pt metal in each of the composite electrocatalyst samples was fixed at 20 wt %.

2.3. Preparation of Working Electrode and Electrochemical Measurements. The working electrodes for electrochemical measurements were fabricated from the ink prepared by ultrasonic dispersion of Pt/C, Pt/CeO_2-H/C, and Pt/CeO_2-HP/C composite powders in 1.0 mL of distilled water and 0.1 mL of Nafion solution (5 wt % solution in a mixture of lower aliphatic alcohols, Sigma-Aldrich), for 30 min. A known volume of the ink composite was then spread onto a mirror-finished glassy carbon electrode (polished with 0.05 μm γ-alumina micropolish, CH Instruments Inc.) of 6 mm diameter (electrode area of 0.28 cm^2) using the micropipet tip. The solvent of the ink was then slowly evaporated (under vacuum) at 40 °C, and in this process, a well-dispersed layer of composite materials on the glassy carbon electrode was obtained. The amount of Pt loading on the glassy carbon electrodes was fixed at 28 $\mu g/cm^2$. All the electrochemical measurements were performed at room temperature using a CHI 7081C electrochemical workstation with a conventional three-electrode configuration. A platinum foil (area = 1 cm^2) and Ag/AgCl electrode (BAS Instruments, USA) were used as the counter and reference electrodes, respectively. A solution consisting of 0.5 M H_2SO_4 and 1 M CH_3OH purged with high-pure Ar for 30 min under constant stirring was taken as a test solution for the electrochemical methanol oxidation study. The final measurement curves were recorded after a stable current response from the working electrodes under continuous cycling at 20 mV s^{-1}. For high reproducibility of the results, a freshly prepared electrolyte solution was used during all electrochemical measurements.

The CO stripping voltammetry was performed in 0.5 M H_2SO_4 solution. After purging the solution with ultrapure Ar for 30 min, gaseous CO (0.1% CO in Ar) was bubbled for 120 min under a fixed potential of 0.0 V vs Ag/AgCl to promote the formation of a perfect CO adlayer on the surface of the electrocatalysts. Excess CO traces from the solution as well as the surface of the electrocatalysts were flushed out by purging the solution with ultrapure Ar for 30 min under an applied potential of 0.0 V vs Ag/AgCl. The CO stripping voltammetry patterns were recorded at a potential scan rate of 20 mV s^{-1}.

2.4. Physicochemical Characterizations. Thermogravimetry analyses were performed on a TA TGA Q500 V20.10 Build 36 instrument under air flow (20 mL/min), with a linear heating rate of 20 °C/min. The thermally induced phase changes of the samples were analyzed on a TA DSC Q200 instrument using open pan mode in air atmosphere. The PXRD patterns were obtained on a Bruker AXS D8 Advance diffractometer at scan rates of 0.01° s^{-1}, using Cu Kα (λ = 0.15408 nm) radiation generated at 40 kV, 30 mA. The crystallite sizes of the samples were approximated using the Scherrer equation, $D = K\lambda/(\beta \cos \theta)$, where D is the linear dimension of the particle (particle size), K is the spherical shape factor (taken as 0.89), and β is the full width at half-maximum height of the peaks.

Multipoint nitrogen adsorption−desorption experiments were carried out at 77 K by means of an automatic Micromeritics ASAP 2020 analyzer using the Brunauer−Emmett−Teller (BET) gas adsorption method. The samples were degassed at 100 °C for 2 h, followed by 150 °C for 10 h in a dynamic vacuum before physisorption measurements. The specific surface area (SBET) values were estimated using software of the instrument based on the BET equation. The porosity distributions in the samples were generated from desorption branches of the isotherms using the Barrett−Joyner−Halenda (BJH) method and a cylindrical pore model.

The high resolution scanning electron microscopy (HRSEM) measurements were carried out using a field emission-gun-equipped FEI Quanta 200 microscope. The sample powders were carefully dispersed on a carbon tape before mounting on the sample holder for HRSEM analysis. The high resolution transmission electron microscopy (HRTEM) measurements were performed on a JEOL 3010 HRTE microscope (lattice resolution of 0.14 nm), fixed with a UHR pole piece and operated at an accelerating voltage of 300 kV. The temperature programmed reduction (TPR) measurements were carried out in a Micromeritics Chemisorb 2750 TPD/TPR system.

For a typical H_2-TPR experiment, 80 mg of the sample loaded in a U-shaped quartz tube was pretreated at 250 °C in flowing 20% O_2/He (25 mL/min) for 1 h and then cooled to room temperature under flowing He. The pretreated sample was then heated to 850 °C at a rate of 10 °C min^{-1}, under the constant flow of 5% H_2/He mixture (20 mL/min), and the TPR patterns were recorded using a thermal conductivity detector.

The X-ray photoelectron spectroscopy (XPS) measurements were carried out using a multiprobe XPS system (Omicron Nanotechnology, Germany) equipped with a dual Mg/Al X-ray source operated at 300 W and 15 kV and a hemispherical analyzer operating in constant analyzer energy (CAE) mode. The spectra were obtained with a pass energy of 50 eV for survey as well as individual scans. The base pressure in the analyzing chamber was maintained at 10^{-10} mbar. The data profiles were subjected to a nonlinear least-squares curve-fitting program with a Gaussian−Lorentzian production function and processed with the Casa XPS program (Casa Software Ltd., U.K.). The adventitious C1s binding energy of 284.9 eV was taken as the reference binding energy for charge correction.

The inductively coupled plasma optical emission spectrometry (ICP-OES) was carried out using a Perkin-Elmer Optima 5300 DV ICP-OES spectrometer to estimate the amount of Pt leaching during preparation of the composite samples. For that, each solid composite sample was digested in aqua regia for 72 h to dissolve the Pt and CeO_2. Undissolved carbon was filtered out, and the filtrate was then diluted with the required amount of triple-distilled water for ICP-OES analysis.

dx.doi.org/10.1021/cs300473e | ACS Catal. 2012, 2, 2795−2809

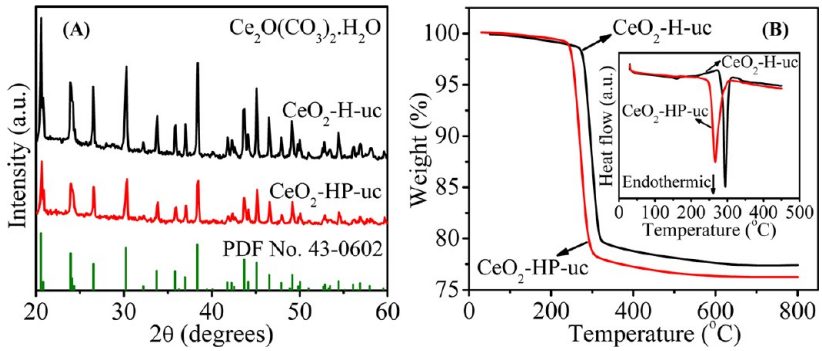

Figure 1. (A) PXRD and (B) TGA profiles of CeO_2-H-uc and CeO_2-HP-uc samples. The inset in part B represents the corresponding DSC profiles of the precursor samples.

3. RESULTS AND DISCUSSION

The powder X-ray diffraction (PXRD) patterns of the uncalcined precursors of CeO_2 are shown in Figure 1A. The formation of pure orthorhombic $Ce_2O(CO_3)_2{\cdot}H_2O$ phase (JCPDS: 44-0617) is confirmed in samples synthesized via polymer-assisted (CeO_2-HP-uc) as well as polymer-free (CeO_2-H-uc) syntheses processes. Under homogeneous precipitation conditions, slow kinetic decomposition of NH_2CONH_2 results in the formation of ionic ammonium cyanate ($NH_4^+ + NCO^-$), which further hydrolyzes in aqueous conditions, releasing OH^- and CO_3^{2-} ions to the solution. The OH^- and CO_3^{2-} ions then coordinate with Ce^{3+} ions in the reaction medium to form $Ce_2O(CO_3)_2{\cdot}H_2O$. The reaction steps during the homogeneous precipitation of $Ce_2O(CO_3)_2{\cdot}H_2O$ is written as[38]

$$NH_2CONH_2 \xrightarrow{\text{hydrolysis}} NH_4^+ + NCO^-$$

$$NCO^- + 3H_2O \rightarrow HCO_3^- + NH_4^+ + OH^-$$

$$HCO_3^- \rightarrow CO_3^{2-} + H^+$$

$$2Ce^{3+} + 2OH^- + 2CO_3^{2-} \rightarrow Ce_2O(CO_3)_2{\cdot}H_2O$$

The intensities of the PXRD peaks of the CeO_2-HP-uc sample are lower as compared with that of CeO_2-H-uc sample, which can be correlated to the lower crystallinity/crystallite size of the CeO_2 sample synthesized via the polymer-assisted method. It is known that the selective surface adsorption properties of polymers prevent agglomeration, frenzied crystal growth, and structural disorganization of nascent crystallites.[44] Similar activity of P123 is supposed to be the reason behind the lower crystallinity/crystallite size of CeO_2-HP-uc.

The CeO_2-H-uc and CeO_2-HP-uc samples were subjected to TG and DSC analyses; the corresponding profiles are shown in Figure 1B. The prototype TG curves of both the precursor samples can be analyzed as two-step weight loss processes, which are assigned as surface dehydration (up to ~250 °C) followed by thermal oxidative decomposition (250−325 °C) of $Ce_2O(CO_3)_2{\cdot}H_2O$. The overall weight losses in CeO_2-H-uc and CeO_2-HP-uc samples are estimated as ~22.6% and ~23.8%, respectively, which indicate varied amounts of adsorbed and crystalline water in the precursor samples. In addition, the oxidative decomposition temperature of the CeO_2-HP-uc sample is marginally lower than that of the CeO_2-H-uc sample. Since the two precursor samples are crystallographically similar, the possible difference in the amount of weight loss and the decomposition temperature can be correlated to the variation in the surface and bulk properties (porosity) of the precursors.

The thermally induced phase changes in the two precursor samples were verified by DSC analysis, and the respective profiles are shown in the inset of Figure 1B. The DSC profile of each sample shows single characteristic endothermic peak within the similar temperature range as observed during the decomposition step in the TG analysis.

The CeO_2-HP-uc and CeO_2-H-uc precursor samples were subjected to thermal treatment, and the products were subjected to PXRD analysis. The PXRD patterns of the calcined samples are shown in Figure 2. The calcined products

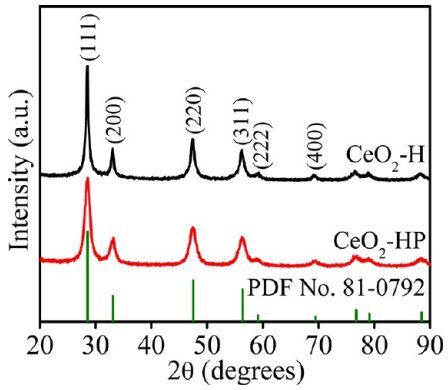

Figure 2. PXRD patterns of CeO_2-H and CeO_2-HP samples.

are perfectly indexed as FCC type CeO_2 (space group of $Fm\bar{3}m(225)$) from the characteristic peaks of the (111), (200), (220), (311), (222), (400), (331), (420), and (422) planes at 2θ values of 28.5, 33.1, 47.5, 56.4, 59.1, 69.4, 76.7, 79.1, and 88.5 degrees (PDF No. 81-0792), respectively. In the PXRD patterns of the CeO_2-HP and CeO_2-H samples, the absence of additional secondary peaks illustrates the complete decomposition of orthorhombic $Ce_2O(CO_3)_2{\cdot}H_2O$ to cubic CeO_2.

In the PXRD patterns, the peaks of the CeO_2-HP sample are marginally broader, which illustrates that the crystallite sizes in the CeO_2-HP sample are smaller as compared with those in the CeO_2-H sample. The average crystallite sizes of the CeO_2-HP and CeO_2-H samples were found to be ~6.8 and 12.3 nm, respectively, calculated from the corresponding (111), (220), and (311) peaks in the PXRD patterns.

The surface morphological characteristics of $Ce_2O(CO_3)_2{\cdot}H_2O$ and the corresponding CeO_2 samples were investigated from FESEM analysis. The FESEM images of the uncalcined precursors and the corresponding calcined samples are shown in Figures 3 and 4, respectively. The FESEM image of the precursor

dx.doi.org/10.1021/cs300473e | ACS Catal. 2012, 2, 2795−2809

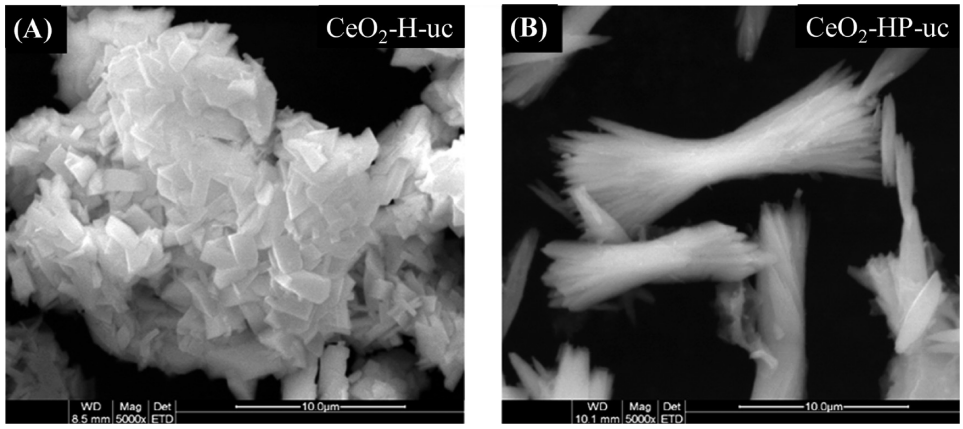

Figure 3. FESEM images of (A) CeO_2-H-uc and (B) CeO_2-HP-uc samples.

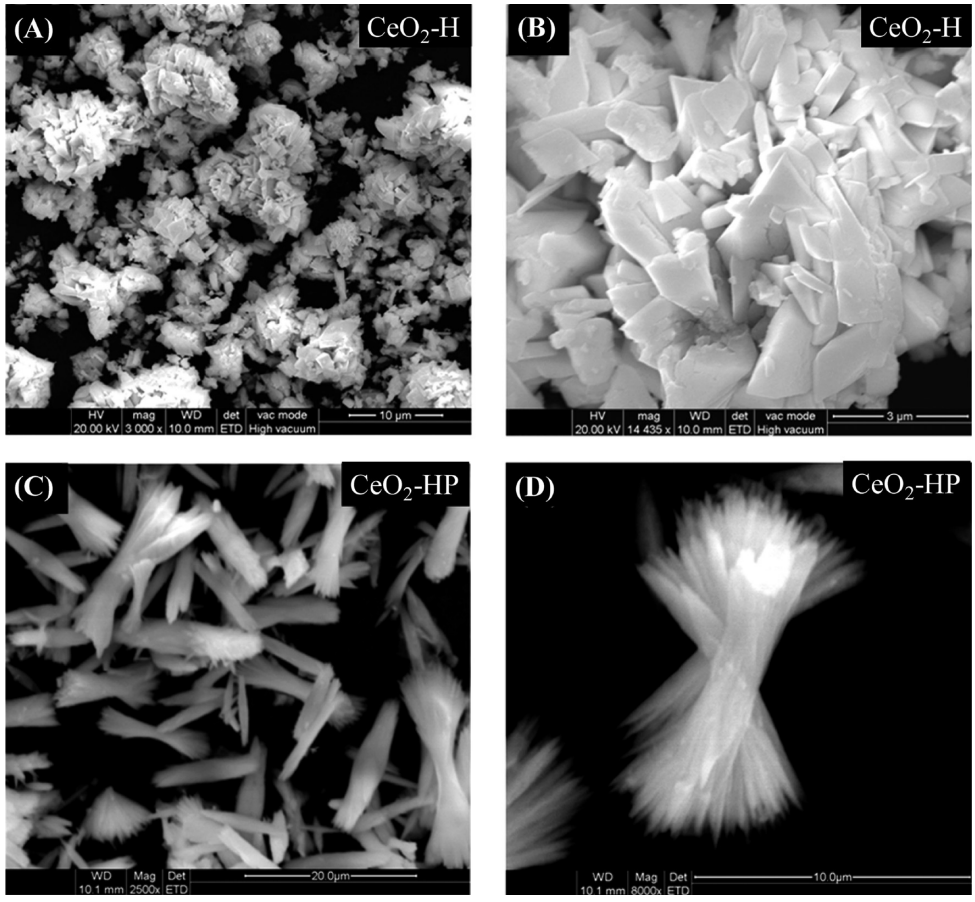

Figure 4. FESEM images of CeO_2-H (A and B) and CeO_2-HP (C and D) samples.

sample synthesized in the polymer-assisted medium shows a completely different surface morphology from the sample synthesized in the polymer-free medium. Furthermore, the surface morphologies of the $Ce_2O(CO_3)_2{\cdot}H_2O$ precursors are highly replicated in the corresponding CeO_2 samples. The surface morphologies of CeO_2-H-uc and CeO_2-H samples show a randomly agglomerated microplate structure, whereas the CeO_2-HP-uc and CeO_2-HP samples show a shuttle-like surface morphology.

It is known that the surface morphology of a material is greatly modulated by the shapes, orientations, and growth of the crystallites that are significantly controlled by the energetic as well as kinetic parameters during synthesis.[45] In effect, the crystal growth and their interactions to larger structures occur in geometric arrangement to minimize the surface energy, and this process is kinetically controlled by the preferential adsorption/desorption of a stabilizer, such as anions and surfactants.[45] Therefore, the formation of a well-defined morphology is controlled by the chemical composition, size, and shape of the primary crystals as well as surface functionality of the nanocrystal surface. In addition, the generation of a specific surface morphology is directly associated with the controlled nucleation and growth process. Since the homogeneous precipitation involves a kinetically controlled nucleation process, because of a slower dissociation and diffusion of precipitating anions to the

dx.doi.org/10.1021/cs300473e | *ACS Catal.* 2012, 2, 2795−2809

solution, the difference in the surface morphology of the CeO_2-H-uc and CeO_2-HP-uc precursors is solely due to the kinetically different crystal-growth and crystal-orientation phenomena.[45,46] The literature shows that under kinetically controlled precipitation, the initial product is the colloidal nanocrystal/seed, which under elevated temperature undergoes nucleation and growth to active monomers and then to nanocrystals.[45−47] The subsequent growth of nanocrystals and their further orientation to a multidimensional structure is kinetically controlled by reduced diffusion and aggregation phenomena. The orientation of nanocrystals to a well-defined structure and further to a superstructure occurs via an oriented attachment (OA) mechanism.[48] The formation mechanisms of $Ce_2O(CO_3)_2{\cdot}H_2O$ precursors and the resulting CeO_2 with different surface morphologies are shown in Scheme 1.

Scheme 1. Plausible Formation Mechanisms of CeO_2-H and CeO_2-HP Microstructures Synthesized in Polymer-Free and Polymer-Assisted Media, Respectively

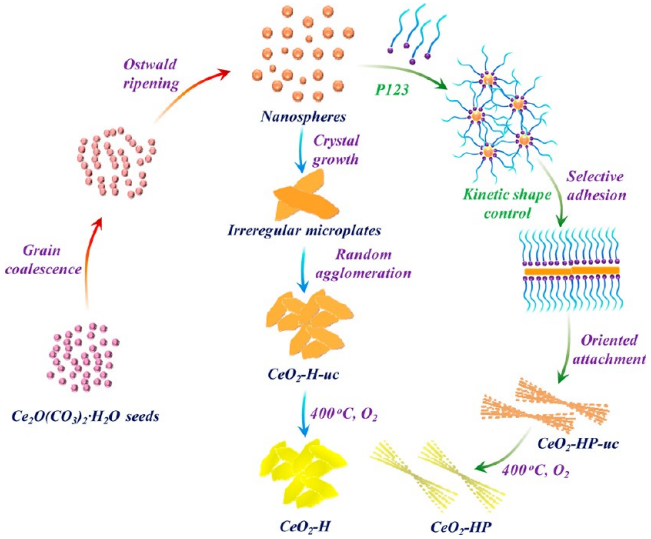

During the homogeneous precipitation process, the kinetically slow nucleation of Ce^{3+} with the OH^- and CO_3^{2-} ions (from the hydrolysis and decomposition of urea) produces $Ce_2O(CO_3)_2{\cdot}H_2O$ seeds, followed by nanocrystals. The nanocrystals then undergo grain-rotation-induced grain coalescence and Ostwald ripening to thermodynamically and symmetrically favorable nanospheres.[48] Further, coherent grain/ripened nanocrystals under selective crystal-facet adhesion of polymer molecules undergo kinetic shape control, leading to the formation of rod-shaped structures. Since facets with high energy grow quicker, the one-dimensional growth of nanorods ceases once the high-energy facet is eliminated due to some complex kinetic and thermodynamic parameters in the reaction medium. Further, the nanorods undergo oriented attachment, resulting in the shuttle-like surface morphology of $Ce_2O(CO_3)_2{\cdot}H_2O$, and the morphology is perfectly retained in the resultant CeO_2. However, in the polymer-free medium, the coalesced/ripened nanocrystals undergo random growth under hydrothermal conditions, leading to the formation of plate-like microcrystals. Under elevated temperature and hydrothermal treatment for a long time, the platelike microstructures tend to decrease the surface energy and randomly agglomerate to bulky microstructures of $Ce_2O(CO_3)_2{\cdot}H_2O$.

The surface area and porosity of the CeO_2-HP and CeO_2-H samples were determined from N_2-sorption measurements and the corresponding N_2 adsorption−desorption isotherms as well as pore size distribution plots are shown in Figure 5A and B, respectively. The characteristic BET isotherms of both CeO_2 samples show type-IV isotherms with H3 type hysteresis loops, essentially demonstrating the presence of slit-shaped pores in the samples, which may be due to the aggregation of platelike particles.[49] The BJH pore size distribution plots in Figure 5B show mono (∼2 nm) and bimodal (∼2 and 6.1 nm) pore size distributions of CeO_2-H and CeO_2-HP samples, respectively, demonstrating the presence of only micropores in the CeO_2-H sample and micro- as well as mesopores in the CeO_2-HP sample.

In the two isotherms, the adsorption in the p/p_0 region of 0 to ∼0.04 indicates the presence of micropores, which generally originate from the bulk of the sample. A closer analysis of the adsorption in the micropore region shows that the volume of N_2 adsorbed by the CeO_2-HP sample is more than that by the CeO_2-H sample. This is basically due to the added micropores in the CeO_2-HP sample, which are from the internal voids between orientationally attached nanorods.[49] In the isotherm plots, small slopes in the adsorption branches and hysteresis between the adsorption−desorption branches are observed in the p/p_0 regions of ∼0.1 to ∼0.8, indicating the presence of large fractions of mesopores, which are mostly from the surface porosity of the samples. A closer look at the N_2 adsorption−desorption curves in the mesopore regions reveals that there is more N_2 adsorption on the CeO_2-HP sample than on the CeO_2-H sample. From the FESEM micrographs (Figure 4), it is evident that, due to orientationally attached nanorods, the surface porosity of the shuttle-shaped CeO_2 is considerably more than that of agglomerated CeO_2. Further, the hysteresis at the macropore region (p/p_0 = ∼0.8 to 1.0) for the CeO_2-HP sample is more prominent as compared with the CeO_2-H sample. The lack of any defined morphology and large

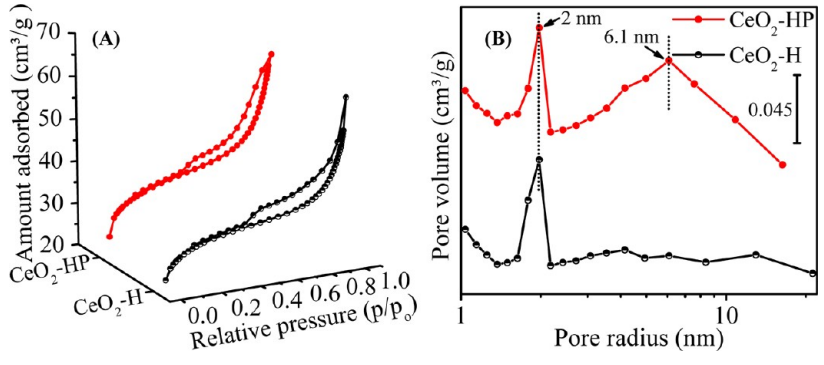

Figure 5. (A) BET isotherms, and (B) BJH pore size distribution profiles of CeO_2−H and CeO_2-HP samples.

dx.doi.org/10.1021/cs300473e | ACS Catal. 2012, 2, 2795−2809

agglomeration of particles could be the reasons behind lower meso- and macroporosity in the CeO_2-H sample. The surface area and porosity of the CeO_2-HP sample (BET surface area 109 m^2 g^{-1}, BJH pore volume 0.11 cm^3 g^{-1}) are found to be superior to the CeO_2-H sample (BET surface area 80 m^2 g^{-1}, BJH pore volume 0.08 cm^3 g^{-1}).

CeO_2 being extensively studied and commercially exploited as a redox catalyst (originated from the Ce^{4+}/Ce^{3+} redox cycle), the ease of reducibility at lower temperature is most significant for its higher catalytic efficiency.[50] Studies show that the reducibility of CeO_2 is promoted by a large surface area, preferential exposure of suitable facets, and surface defects such as oxygen vacancies.[29,51] Further, the amount and density of oxygen vacancies are largely dependent upon the surface structures and crystal characteristics of the materials. In this context, H_2-TPR is one of the best-studied methods to determine the amount, density, and labiality of oxygen vacancy in the CeO_2 lattice.[52]

The shuttle-shaped CeO_2 bears a unique surface structure and smaller crystallite size as compared with the bulk CeO_2 sample. Hence, the nature of effective oxygen vacancies is expected to be distinctive in shuttle-shaped CeO_2. Therefore, the CeO_2-HP and CeO_2-H samples were subjected to H_2-TPR analyses, and the corresponding reduction profiles are shown in Figure 6. The H_2 TPR profiles of both the CeO_2 samples show

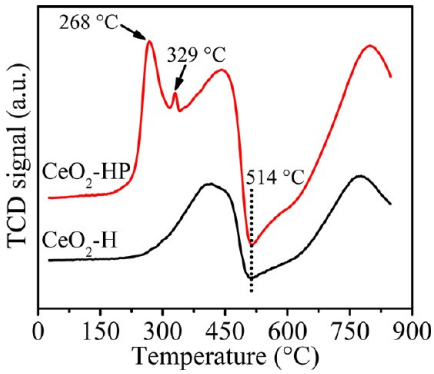

Figure 6. H_2-TPR profiles of CeO_2-HP and CeO_2-H samples.

two major reduction peaks: the lower temperature peak (below 600 °C) due to a reduction of surface capping oxygen and the higher temperature peak (above 600 °C) due to reduction of bulk oxygen.[50,51] In fact, the low-temperature reduction profile of CeO_2 is of special interest, since it is the signature of the material to be a better catalyst for low-temperature oxidation reactions. The CeO_2-H sample shows a typical two-peak reduction profile at ~420 and 770 °C; however, the CeO_2-HP sample shows a unique, highly intense low-temperature reduction peak at ~268 °C. From the H_2-TPR peak intensities, it is seen that the H_2 consumption for surface reduction of the CeO_2-HP sample is significantly higher than the CeO_2-H sample. Recently, Zhou et al., have shown similar low-temperature H_2-reducibility of CeO_2 nanotubes.[53] However, the low temperature reduction peak intensity in CeO_2 nanotubes was minor when compared with the peak from the major reduction of surface capping oxygen.

In shuttle-shaped CeO_2, the low temperature reduction peak is significantly more intense as compared with the other reduction peaks. This can be attributed to the presence of a larger size and number of oxygen vacancy clusters as well as a large amount of reactive oxygen species on the surface of the shuttle-shaped CeO_2.[50−53] Since the migration of oxygen in ceria takes place via a vacancy hopping mechanism, linear surface oxygen vacancies are favorable for migration of oxygen, which enhances the reducibility of CeO_2.[54] Hence, it can be envisaged that, the shuttle-shaped CeO_2 possess higher numbers of linear surface oxygen vacancy clusters. Furthermore, the presence of oxygen vacancy clusters may facilitate effective adsorption sites for oxygen-rich molecules and can play a more functional and effective role in catalytic application. The negative peaks at ~514 °C in the TPR profiles of both samples are assigned to the thermal desorption of H_2 from the porous CeO_2 samples, release of CO and CH_4 during the reduction of surface carbonates, or both.

Ceria being a good promoter to Pt/C for alcohol oxidation in DMFC applications, the CeO_2-HP and CeO_2-H samples were tested for their promoting efficiency toward methanol electrooxidation reaction.[28,30−37] In this context, CeO_2-HP- and CeO_2-H-loaded Pt/C catalysts were subjected to physical as well as electrochemical characterization. The corresponding PXRD patterns of Pt/C, Pt/CeO_2-H/C and Pt/CeO_2-HP/C samples are shown in Figure 7. The Pt/C sample shows major diffraction

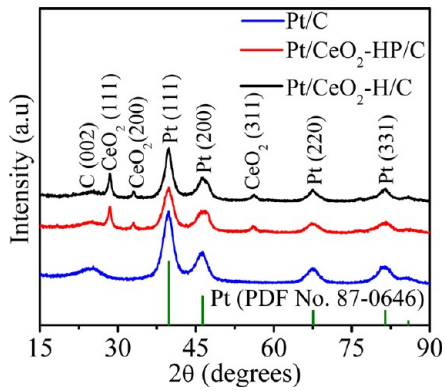

Figure 7. PXRD patterns of Pt/C, Pt/CeO_2-HP/C and Pt/CeO_2-H/C samples.

peaks at 2θ values of 39.8°, 46.3°, 67.6°, and 81.4° corresponding to the (111), (200), (220), and (331) planes of metallic Pt with fcc crystal lattice. The diffraction patterns of the composites also show characteristic peaks of CeO_2. However, not all the peaks of CeO_2 could be identified in the Pt/CeO_2-H/C and Pt/CeO_2-HP/C composites, since some of the diffraction peaks of Pt and CeO_2 appear in similar 2θ positions. Broad peaks at a 2θ value of ~24.9° are the signatures of (002) diffraction of the graphitic Vulcan XC-72 carbon support in the samples. As compared with Pt/C, the characteristic diffraction peaks of Pt in Pt/CeO_2-H/C and Pt/CeO_2-HP/C samples are broader and less intense. This is due to a smaller crystallite size and better dispersion of Pt on the CeO_2-containing samples. From Figure 7, it is seen that Pt peaks in the Pt/CeO_2-HP/C sample are broader than those in the Pt/CeO_2-H/C sample. These observations suggest that Pt dispersion is better in the presence of the shuttle-shaped CeO_2 (CeO_2-HP sample) as compared with bulk CeO_2. This was further probed by HRTEM analysis. The corresponding microscopic images of Pt/C, Pt/CeO_2-HP/C and Pt/CeO_2-H/C samples are presented in Figure 8.

In the Pt/C sample (Figure 8A), the crystallites of Pt are agglomerated, whereas in the CeO_2-containing Pt/C samples (Figure 8B and C), the Pt particles are uniformly dispersed. Further, dispersion of Pt in the shuttle-shaped CeO_2-containing

dx.doi.org/10.1021/cs300473e | ACS Catal. 2012, 2, 2795−2809

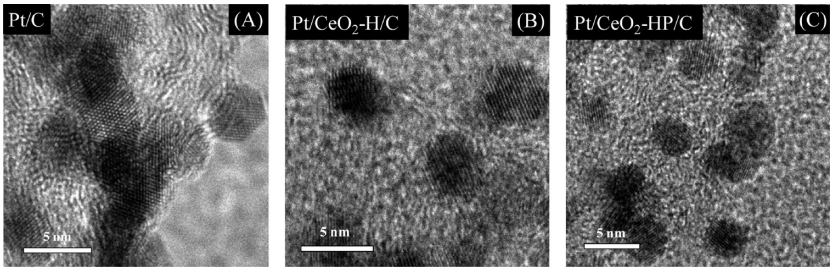

Figure 8. HRTEM images of Pt crystallites in (A) Pt/C, (B) Pt/CeO_2-H/C, and (C) Pt/CeO_2-HP/C samples.

sample (Figure 8C) is more uniform as compared with the Pt particles in the bulk CeO_2-containing sample (Figure 8B). It is known that CeO_2 promotes uniform dispersion and maintains a smaller particle size of supported metals.[40] Further, the surface morphology of CeO_2 influences the nature of the Pt dispersion, and in this context, the nanostructured CeO_2 with a high surface area may be a better substrate for improved dispersion of Pt particles as compared with the bulk CeO_2 with lower surface area. From the HRTEM images, the sizes of the Pt crystallites in the Pt/CeO_2-HP/C sample are estimated to be ~3.7 nm, which is smaller than the Pt crystallites of size ~4.3 nm in the Pt/CeO_2-H/C sample. These crystallite sizes are in close concurrence with the Pt crystallite sizes of ~3.5 nm and ~4.3 nm, estimated from the corresponding Pt (220) planes (from PXRD patterns) of Pt/CeO_2-HP/C and Pt/CeO_2-H/C samples, respectively.

Earlier studies reveal that CeO_2 possesses a positive charge if present in a medium with pH < 6, whereas it acquires a negative surface charge if present in a medium with pH > 7.8.[37] In this study, the reactions between Pt, carbon black, and CeO_2 were performed in media with a pH of ~10; hence, the surfaces of the CeO_2 particles are expected to be negatively charged. It is theoretically predicted that the noble-metal atoms preferentially get adsorbed at the anion sites on CeO_2 surface.[55] In particular, Pt atoms typically get adsorbed on the surface O-bridge sites.[41,55,56]

Since in this study, the reactions were carried out in highly basic media, the surface of the CeO_2 samples acquires a higher negative charge for the preferential surface adsorption of Pt. This leads to energetically favorable electrostatic interactions between Pt atoms and CeO_2 surface. Because of the high surface area and nanodimentional structure, the shuttle-shaped CeO_2 may expose a uniform active surface, leading to a larger negative charge, which offers a stronger interaction with Pt particles. In addition, a polar solvent, such as ethylene glycol (EG), performs a dual role of reducing the H_2PtCl_6 to Pt and enhancing the dispersion of CeO_2 on Vulcan XC-72 carbon black.

Thermodynamically, a reaction temperature of >113 °C is essential for the reduction of H_2PtCl_6 by EG. During a microwave-mediated reaction in a domestic microwave oven at 1200 W, the temperature of the medium reaches ~200 °C, which is quite adequate for rapid reduction of H_2PtCl_6 to Pt. The homogeneous microwave heating in the presence of EG also helps in the faster reduction and better dispersion of Pt particles on CeO_2/C supports. The defect sites on the oxide surface also help in the heterogeneous nucleation of the Pt^{2+} intermediate and its stepwise reduction to Pt^0.[57] Since, from the TPR analysis, the shuttle-shaped CeO_2 was found to have a larger number of surface oxygen vacancies, the rate of heterogeneous nucleation of Pt^{2+} and its further reduction to Pt^0 is expected to be higher on the surface of shuttle-shaped CeO_2 as compared with that on the bulk CeO_2. From ICP-OES analysis, the amounts of Pt and CeO_2 in the Pt/C, Pt/CeO_2-H/C, and Pt/CeO_2-HP/C samples were estimated to be ~99.95–99.97% of the actually loaded amounts, which suggests negligible leaching of Pt and CeO_2 during the preparation of the composites.

The oxidation states of Pt and Ce in the Pt/CeO_2-HP/C sample were investigated by XPS analysis. Figure 9 shows the

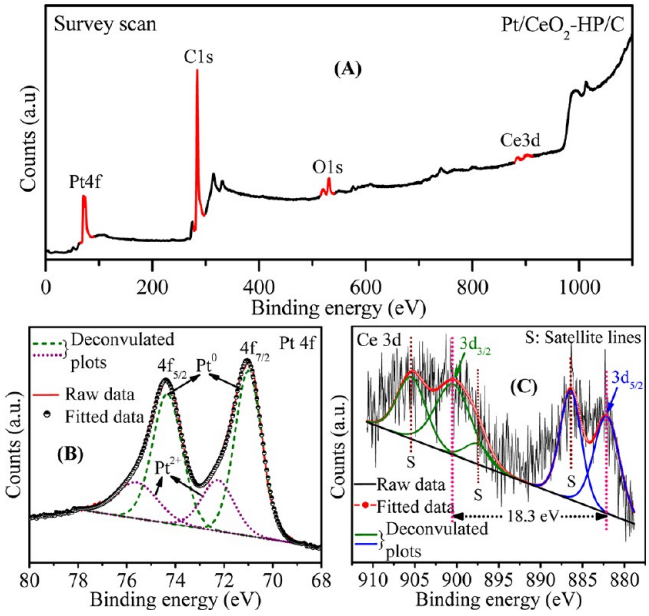

Figure 9. (A) XPS survey scan, (B) Pt 4f and (C) Ce 3d core level spectra of Pt/CeO_2-HP/C sample. Deconvoluted XPS profiles are also shown in the respective figures.

XPS survey scan and Pt 4f as well as Ce 3d core level regions. In the survey scan (Figure 9A), the peaks due to C 1s, O 1s, Ce 3d, and Pt 4f are identified clearly in the respective binding energy regions. The Pt 4f region in Figure 9B shows a doublet peak with binding energies at 71.0 and 74.35 eV, which are the signatures of the Pt^0 state.[24,27,57] The spin–orbit splitting energy of ~3.35 eV matches well with the reported values.[58] This shows that the predominant species in the Pt/CeO_2-HP/C sample is Pt^0. Further, the deconvolution of the Pt 4f peaks shows peaks at binding energies of 72.27 and 75.65 eV, which are the signature of Pt^{2+} species. This is attributable to the presence of PtO/$Pt(OH)_2$ species in the composites.[24,27,57] However, the presence of PtO/$Pt(OH)_2$ species is trivial; they are commonly present on the surface of ultrafine Pt particles. The deconvolution of the Pt 4f region does not show any peaks pertaining to the presence of Pt^{4+}, which clearly implies the complete reduction of H_2PtCl_6 to Pt by EG, during the microwave treatment.

The Ce 3d region (Figure 9C) shows weak doublets corresponding to the spin–orbit split of 3d core holes and the

dx.doi.org/10.1021/cs300473e | ACS Catal. 2012, 2, 2795–2809

associated satellites.[28,30−37,57,59] The peaks at binding energies of 882.15 and 900.53 eV in the deconvoluted spectra correspond to the $3d_{5/2}$ and $3d_{3/2}$ states of Ce^{4+}, respectively, with spin−orbit splitting of 18.38 eV. The satellite peak at 897.43 eV, associated with the Ce $3d_{3/2}$ state, is due to the Ce $3d^94f^0$ O $2p^6$ final state, which is characteristic of Ce^{4+}. Further, the satellite peaks located at binding energies of 886.35 and 905.45 eV correspond to the Ce $3d^94f^1$ O $2p^5$ final state, showing the presence of Ce^{4+} in the composite. In CeO_2, the prominent satellite peaks are essentially due to shake-down (energy gain) processes and are called "shake-down states".[60] The ill-defined valley between the $3d_{5/2}$ (882.2 eV) and satellite (886.4 eV) doublet in the XPS profile of Ce 3d is assigned to the Ce $3d^94f^1$ O $2p^6$ final state, indicating the presence of some small amount of Ce^{3+} in the composite.[61] Since the Pt/CeO_2-H/C sample was synthesized under experimental conditions identical to those for the Pt/CeO_2-HP/C sample, the chemical states of Pt and CeO_2 in the Pt/CeO_2-H/C sample are supposed to be essentially similar to those in the Pt/CeO_2-HP/C sample.

The electrocatalytic efficiencies of the Pt/CeO_2-H/C and Pt/CeO_2-HP/C samples were evaluated by sweep voltammetry, chronopotentiometry, and chronoamperometry measurements in a 0.5 mol L^{-1} H_2SO_4 solution and compared with the efficiency of the Pt/C sample. The typical cyclic voltammograms in Figure 10A show peaks corresponding to hydrogen adsorption/desorption, double-layer charging, oxide formation, and oxide reduction on the Pt surface.[62,63] The CV behavior of the samples in the potential region of −0.2 to 0.2 V (vs Ag/AgCl) are basically associated with H_{upd} (underpotentially deposited hydrogen) processes ($H^+ + e^- = H_{upd}$).[62−64] Beyond 0.4 V in the anodic scan, the characteristic CV behaviors of the samples are due to the formation of OH_{ad} (adsorbed hydroxyl species; $2H_2O = OH_{ad} + H_3O^+ + e^-$), which creates ordered layers of $PtO_x{\cdot}nH_2O/Pt(OH)_y{\cdot}nH_2O$ ($x = 1, 2$; $y = 2, 4$) on the metallic Pt surface.[63] During the reverse scans, the CV patterns in the region of 0.8−0.2 V appear as a result of the corresponding reduction of $PtO_x{\cdot}nH_2O/Pt(OH)_y{\cdot}nH_2O$ species.

The voltammetric behaviors of CeO_2-promoted Pt/C samples are certainly different from the Pt/C sample, especially in the H_{upd} regions. Interestingly, the hydrogen adsorption/desorption patterns of Pt/C sample are quite broad as compared with those of CeO_2-promoted samples. The characteristic peaks in the H_{upd} regions of CeO_2-promoted samples appear distinct and sharp.

It is known that the hydrogen adsorption/desorption behavior on a Pt surface is highly structure-sensitive.[15,65] Particularly, in CeO_2-promoted samples, the sharp peak at −0.1 V in the anodic scan (peak 1 in Figure 10D) is a signature of H on the (110) step, the peak at 0.02 V in the anodic scan (peak 2 in Figure 10D) is a signature of H on the (100) step, and the broad peak in the region of 0.5−1 V (peak 3 in Figure 10D) is the signature of anions on the (111) domain.[66] From the voltammetric profiles in the H_{upd} and anion adsorption regions of CeO_2-promoted Pt/C samples, it is quite clear that the Pt particles in these composites expose selective facets for interaction with H and other anions.[65,66] In contrast, the Pt particles in the Pt/C sample do not selectively expose any specific faces for molecular interaction. Further, peaks in the H_{upd} regions for CeO_2-promoted Pt/C samples are distinctly sharp as compared with those for the Pt/C sample, which clearly indicates the higher number and better cleanliness of the selectively exposed Pt surfaces in the CeO_2-promoted samples.[62,63,65,66]

From the HRTEM images in Figure 8, it can be clearly observed that in the Pt/C sample (Figure 8A), the Pt crystallites randomly expose different lattices planes, whereas in the Pt/CeO_2-H/C (Figure 8B) and Pt/CeO_2-HP/C (Figure 8C) samples, only specific lattice planes of Pt crystallites are exposed. Further, among the CeO_2-promoted samples, the peaks in the H_{upd} regions of the shuttle-shaped CeO_2-promoted sample are

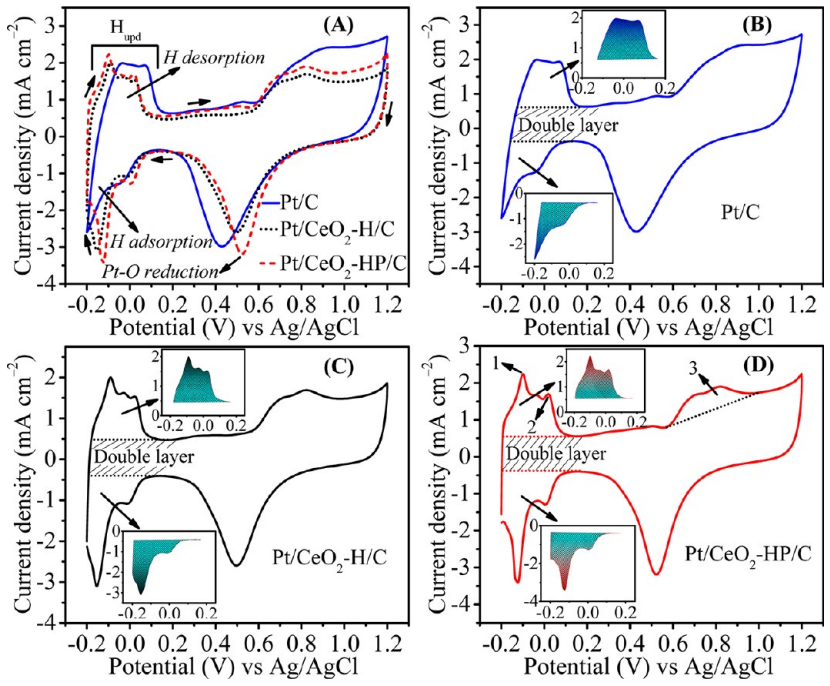

Figure 10. (A) Comparative cyclic voltammograms (scan rate = 20 mV s^{-1}) of Pt/C, Pt/CeO_2-H/C, and Pt/CeO_2-HP/C samples in 0.5 mol L^{-1} H_2SO_4 solution. (B−D) Individual cyclic voltammograms of the samples showing the integrated hydrogen adsorption and desorption peaks in the insets.

dx.doi.org/10.1021/cs300473e | ACS Catal. 2012, 2, 2795−2809

better defined and sharp, which essentially shows a better exposed and higher number of specific lattice planes of the Pt crystallites. This observation is in concurrence with the fact that, due to more exposed uniform surface sites of the shuttle-shaped CeO_2, the crystal growth of Pt on the surface of CeO_2 is highly homogeneous, with geometrically controlled Pt facets. In addition, a higher number of oxygen vacancies on the surface of the shuttle-shaped CeO_2 argue for better interaction between Pt and the surface O-bridge sites of CeO_2. However, in the bulk CeO_2, the exposed active surface sites for interaction with growing Pt crystallites are fewer in number and irregular in nature. In addition, the bulk CeO_2 surface bears smaller numbers of oxygen vacancies for interaction with growing Pt crystals. Further, the anodic and the cathodic peaks in the H_{upd} regions of CeO_2-promoted Pt/C samples are more symmetrical than the Pt/C sample. This essentially indicates a faster and more reversible Volmer reaction on CeO_2-promoted Pt/C samples. It further suggests the interfacial promoting activity of CeO_2 for controlled and specific crystal growth of Pt favors the electrochemical reactivity of Pt toward hydrogen.[67]

The higher symmetric peak profiles in the H_{upd} regions of CeO_2 promoted Pt/C samples are also indicative of a highly reversible hydrogen adsorption/desorption process as compared with that on the Pt/C sample.[67−69] From Figure 10A, it is seen that the voltammetric current responses of the samples in the H_{upd} region are different. Since the Pt loading in all the samples is the same, the variation in the current response is attributed to the difference in the number of electroactive sites in the samples for hydrogen electroadsorption/desorption. Essentially, this is represented as the actual electrochemical active surface area (EAS) of the samples, which can be determined from the Coulombic charge for hydrogen adsorption/desorption (Q_H) in the H_{upd} region of the cyclic voltamogram, assuming a hydrogen adsorption stoichiometry of one (i.e., one adsorbed H per active Pt surface atom). Here, the Q_H was determined using the expression, $Q_H = 0.5 \times (Q_{total} - Q_{DL})$, where Q_{total} is the total charge transfer in the hydrogen adsorption/desorption potential region and Q_{DL} is the charge from double-layer charging of Pt and Vulcan XC-72.[70] The potential versus current density plots in the H_{upd} regions of each sample were integrated (insets of the Figure 10B, C, D) to estimate Q_H, which were then used to calculate the EAS of individual samples. The Coulombic charge (Q_H) during hydrogen adsorption/desorption in the Pt/C, Pt/CeO_2-H/C, and Pt/CeO_2-HP/C samples were estimated to be 0.246, 0.287, and 0.303 mC cm^{-2}. The EAS of Pt nanocrystals in the individual catalysts were estimated using the following expression:[71]

$$\text{EAS}\ (m^2 g^{-1}) = \frac{Q_H}{0.21 \times M_{Pt}}$$

where 0.21 mC cm^{-2} is the electrical charge associated with monolayer adsorption of hydrogen/charge required to oxidize a monolayer of H on a polycrystalline Pt electrode (assuming surface density of 1.3×10^{15} atoms cm^{-2}) and M_{Pt} is the Pt loading on the working electrodes (0.028 mg cm^{-2}). The EAS of Pt nanocrystals in Pt/C, Pt/CeO_2-H/C, and Pt/CeO_2-HP/C samples was estimated to be 42, 48, and 51 m^2 g^{-1}, respectively. This clearly shows that, irrespective of similar Pt loading on each sample, the EAS for the CeO_2-promoted Pt/C samples was higher than the bare Pt/C sample. Further, the shuttle-shaped CeO_2-promoted Pt/C sample is higher than the bulk CeO_2-promoted Pt/C sample. This is due to the smaller size and highly dispersed nanoparticles of Pt in the CeO_2-promoted Pt/C samples. Further, unlike bulk CeO_2, higher amounts of suitably exposed lattice planes and a higher number of defects are present on the nanostructured shuttle-shaped CeO_2, which promote geometrically controlled growth of smaller and multifaceted Pt crystallites on its surface.[40] Unlike in bare Pt/C and bulk CeO_2-promoted Pt/C, the interaction between the Pt nanoparticles and the shuttle-shaped CeO_2 is stronger, which essentially prevents migration and agglomeration of Pt nanoparticles. The smaller and highly dispersed Pt crystallites also expose a larger number of active sites for surface reactions. This is clear from the hydrogen electrosorption during CV measurements, which shows a higher electroactive surface area of Pt crystallites dispersed on the shuttle-shaped CeO_2-promoted Pt/C sample as compared with bulk CeO_2-promoted Pt/C and bare Pt/C samples.

It is known that a catalyst with larger EAS usually possesses higher electrocatalytic activity.[72] Therefore, the methanol electrooxidation activity of shuttle-shaped CeO_2 as well as bulk CeO_2-promoted Pt/C samples were studied and compared with the activity of the Pt/C sample to understand the effect of the surface morphology of CeO_2 on the electrocatalytic activity. The current response of methanol electrooxidation during CV measurements on Pt/C, Pt/CeO_2-H/C, and Pt/CeO_2-HP/C samples in 0.5 mol L^{-1} H_2SO_4 + 1 M CH_3OH solution, each at scan rates of 20 mV s^{-1}, are shown in Figure 11. During initial anodic potential sweeps, broad peaks are observed, corresponding

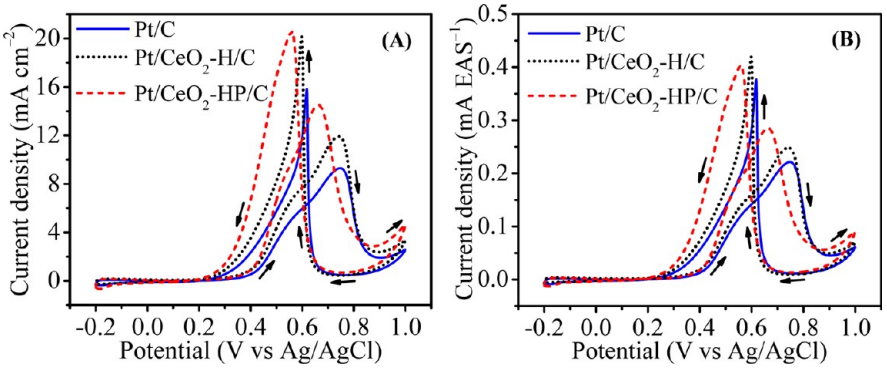

Figure 11. Cyclic voltammograms of Pt/C, Pt/CeO_2-H/C, and Pt/CeO_2-HP/C sample electrodes in 0.5 mol L^{-1} H_2SO_4 + 1 M CH_3OH solution at scan rates of 20 mV s^{-1}. (A, B) Current response with respect to geometrical area of the electrode (cm^2) and per unit electroactive surface area (m^2) of the catalyst samples, respectively.

dx.doi.org/10.1021/cs300473e | ACS Catal. 2012, 2, 2795−2809

to the formation and oxidation of Pt-$(CH_3OH)_{ads}$ on the catalyst surface which can be represented as[73]

$$CH_3OH + Pt\square \rightarrow Pt(CH_3OH)_{ads}$$
$$\rightarrow 4H^+ + 4e^- + Pt{-}CO$$

where $\square$ denotes a single Pt site for CH_3OH adsorption and oxidation during anodic scan. Since Pt is highly prone to poisoning by CO, the active Pt sites are blocked during the anodic sweep, hindering further reaction. The CO-blocked Pt sites need regeneration by the removal of CO to keep the Pt catalyst active for further CH_3OH electrooxidation. This process is represented as

$$Pt{-}CO + H_2O \rightarrow Pt + CO_2 + 2H^+ + 2e^-$$

During reverse potential sweeps (cathodic), sharp peaks with positive current density are attributed to the removal of carbonaceous species adsorbed on the catalyst surface or reoxidation of methanol due to the reduction of platinum oxide.[74] The carbonaceous species are linearly bonded C═O that strongly adsorb on Pt surface (Pt−C═O) up to a saturation coverage of ∼0.68, depending upon the exposed active planes.[75]

From the anodic peak current densities in Figure 11A, it is observed that the CeO_2-promoted Pt/C catalysts exhibit higher coated area-specific peak current than the Pt/C sample. In addition, the shapes of cathodic peaks and the corresponding current densities are quite different. This is due solely to the difference in efficiency of CO removal and their diffusion kinetics during the cathodic scan. The anodic (forward) methanol oxidation peak of the Pt/CeO_2-HP/C sample electrode occurs at 0.66 V (vs Ag/AgCl), which is ∼8 and ∼9 mV lower than the peak potentials of Pt/CeO_2-H/C and Pt/C samples, respectively. Similarly, the cathodic (backward) peak of the Pt/CeO_2-HP/C sample electrode occurs at 0.55 V (vs Ag/AgCl) which is ∼0.04 and ∼0.06 V lower than the peak potentials of the Pt/CeO_2-H/C and Pt/C samples, respectively.

Essentially, strongly adsorbed carbonaceous species inhibit further MeOH adsorption, which diminish the specific current density at a given potential, and shift the oxidation to positive potentials.[10] Hence, the methanol oxidation as well as removal of carbonaceous species at lower overpotential indicates better electrocatalytic activity of the material.[10,69] The lower oxidation peak potential of the Pt/CeO_2-HP/C sample as compared with the Pt/CeO_2-H/C and Pt/C samples indicates higher promoting activity of shuttle-shaped CeO_2 as compared with the bulk CeO_2 for the methanol electrooxidation reaction. This is further supported by a higher coated area-specific anodic peak current density of the Pt/CeO_2-HP/C sample (14.6 mA cm^{-2}) as compared with the Pt/CeO_2-H/C (11.9 mA cm^{-2}) and Pt/C (9.4 mA cm^{-2}) samples.

To further elucidate the shape-selective-promoting activity of CeO_2, the coated area-specific methanol electrooxidation currents were normalized with the electroactive surface area of Pt, which is presented in Figure 11B. Interestingly, the EAS specific anodic peak current density of the Pt/CeO_2-HP/C sample (0.286 mA EAS^{-1}) is higher than that of the Pt/CeO_2-H/C (0.248 mA EAS^{-1}) and Pt/C (0.222 mA EAS^{-1}) samples, which clearly demonstrates the shape-selective-promoting activity of CeO_2 to Pt/C for the methanol electrooxidation reaction. In the context of mechanistic understanding, the literature shows that a $(OH)_{ads}$ species is required for the removal of adsorbed CO on Pt during the methanol electrooxidation reaction.[18−20] In this perspective, the literature also shows that the promoting effect of CeO_2 for Pt/C is due to the synergic effect of CeO_2, through which triple-phase interfacial (interface between the Pt, oxide, and the electrolyte[76,77]) OH groups react with absorbed CO on Pt particles, producing CO_2 via a bifunctional mechanism. This phenomenon is essentially responsible for improving the CO tolerance of the CeO-promoted catalysts.[28,30−37] The bifunctional mechanism on a Pt/CeO_2 system is represented as follows:

$$CeO_2 + H_2O \rightarrow CeO_2{-}OH_{ads} + H^+ + e^-$$
$$Pt{-}CO_{ads} + CeO_2{-}OH_{ads} \rightarrow Pt + CeO_2 + CO_2 + H^+ + e^-$$
and/or
$$Pt{-}CeO_2 + xCO \rightarrow Pt{-}CeO_{2-x} + xCO_2$$

It is known that the promotional effect of CeO_2 is essentially a surface phenomenon, since a triple-phase interface is significant for generation of OH_{ads} and its further interaction with adjacent CO_{ads} on Pt.[28,30−37,78] In this context, the surface morphology and crystallographic characteristics of CeO_2 are expected to control the number of triple-phase interfaces and the resultant number of OH_{ads} for removal of adjacent CO_{ads} on Pt. Crystalline CeO_2 with a higher concentration of oxygen vacancies (defects) is suitable for high oxygen mobility and stabilization of surface oxygen-containing species such as OH, which can activate and oxidize the adsorbed CO more efficiently. As observed from the TPR analysis, the shuttle-shaped CeO_2, because of the hierarchical morphology, bears more oxygen vacancies (defects) than the bulk CeO_2. Therefore, the oxygen mobility of OH_{ads} on the surface of the shuttle-shaped CeO_2 is more pronounced than on the bulk CeO_2 surface. The hierarchical shuttle-shaped surface morphology of CeO_2 with a higher surface area, oxygen vacancies, and identical atomic ensembles possesses an added triple-phase interfacial region for higher concentrations of strongly adsorbed OH groups. This, in effect, boosts the conversion of absorbed CO to free CO_2 on the Pt/CeO_2-HP/C sample.

The higher electrocatalytic CO_{ads} oxidation efficiency of the shuttle-shaped CeO_2-promoted Pt/C was investigated further using CO-stripping voltammetry. The results are compared with the efficiencies of bulk CeO_2-promoted Pt/C and bare Pt/C samples in Figure 12. From the CO stripping voltammetry profiles of all the samples (Figure 12A, B, C), it is clearly seen that the electrooxidation of CO_{ads} occurs in the very first cycle. In the second cycle, the characteristic peaks appear in the usual H_{upd} region as a result of the desorption of hydrogen (adsorbed on the clean Pt surface in the anodic scan of the first cycle), which essentially indicates complete oxidation of adsorbed CO and generation of clean Pt sites during the first (anodic) scan. The comparative current responses of the various samples during CO electrooxidation, shown in Figure 12D, demonstrate (i) the higher current density of the CeO_2-promoted Pt/C samples as compared with the Pt/C sample and (ii) negative shifts in the CO_{ads} electrooxidation peak potentials of CeO_2-promoted Pt/C samples as compared with the Pt/C sample. In addition, the corresponding CO electrooxidation current density (5.39 mA cm^{-2}) and magnitude of the negative shift (0.09 V) in the CO electrooxidation peak potential of the shuttle-shaped CeO_2-promoted Pt/C are clearly higher than that of bulk CeO_2-promoted Pt/C (current density = 4.51 mA cm^{-2}, negative shift in peak potential = 0.07 V). This indicates the formation of OH_{ads} species at lower potential and the better electronic promoting activity of the shuttle-shaped CeO_2 in weakening the Pt−CO bond, which essentially lower the

dx.doi.org/10.1021/cs300473e | ACS Catal. 2012, 2, 2795−2809

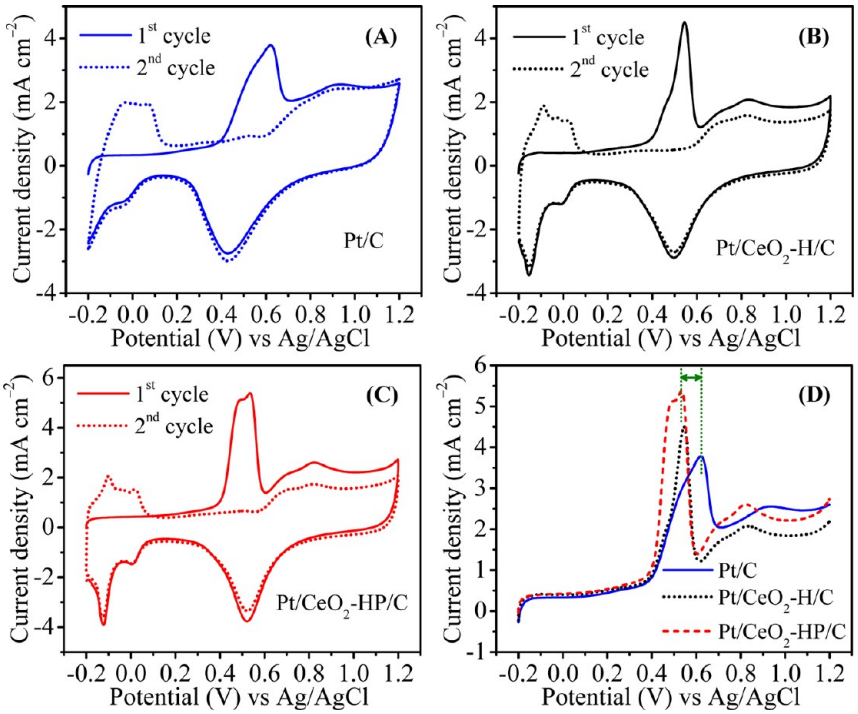

Figure 12. Comparative CO stripping voltammograms (first and second cycles) of (A) Pt/C, (B) Pt/CeO_2-H/C, and (C) Pt/CeO_2-HP/C sample electrodes in 0.5 mol L^{-1} H_2SO_4 solution at scan rates of 20 mV s^{-1}. (D) Comparative current response during CO stripping on various sample electrodes.

overpotential and exhibit a higher negative shift in the onset potential and CO electrooxidation peak potentials.[28,30−37,78,79] Since the electrooxidation of CO molecules is a site-specific phenomenon, the larger and uniform atomic ensembles present on the uniformly grown shuttle-shaped CeO_2 also assist the efficient oxidation of CO to CO_2.[80,81] In addition, the higher CO electrooxidation current density exhibited by the Pt/CeO_2-HP/C sample basically shows higher number of adsorbed OH species on the surface of the shuttle-shaped CeO_2, which consequently oxidize more CO to CO_2. In addition, the CO stripping peaks of the Pt/CeO_2-H/C and Pt/CeO_2-HP/C samples are narrower compared with that of the Pt/C sample electrode, which clearly indicates the promoting activity of CeO_2 in the electrocatalytic oxidation of CO_{ads}.[10]

The schematic representation of enhanced CO electrooxidation on the shuttle-shaped CeO_2-promoted Pt/C due to a higher number of adsorbed OH species as compared with bulk CeO_2-promoted Pt/C is shown in Scheme 2.

The antipoisoning ability of the catalysts for methanol electrooxidation reaction was studied using chronopotentiometry measurements since it is a measure of the constant current operation efficiency of the fuel cell.[62] In this context, the steady-state measurements at a constant current density polarization of 15 mA cm^{-2} were conducted on the Pt/C and CeO_2-promoted Pt/C sample electrodes. From the chronopotentiometry patterns of all the samples in Figure 13, it is observed that the potentials gradually increase with polarization time and finally jump to limiting values, which is due to oxygen evolution rather than methanol electrooxidation, essentially indicating poisoning of the catalyst.[28] During methanol electrooxidation, CO as well as intermediate CHO molecules get adsorbed onto the surface of the electrocatalyst, which largely reduces its catalytic durability. To compensate for the applied anodic current density, a potential jump to a higher value (~1.1 V) occurs, where H_2O gets electrolyzed and oxygen evolution takes place. In this process, the time required for the potential jump is taken as a

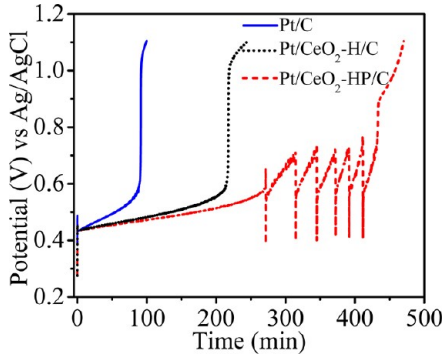

Figure 13. Potential vs time (chronopotentiometry) profiles of Pt/C, Pt/CeO_2-H/C, and Pt/CeO_2-HP/C sample electrodes in 0.5 mol L^{-1} H_2SO_4 + 1 M CH_3OH solution at a fixed current density of 15 mA cm^{-2}.

Scheme 2. Representation of CO_{ads} (on Pt) Oxidation by OH_{ads} (on CeO_2) by (A) Shuttle-Shaped CeO_2 and (B) Bulk CeO_2

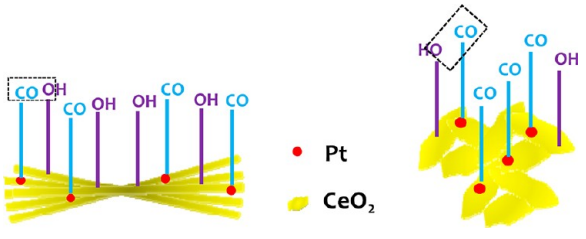

dx.doi.org/10.1021/cs300473e | ACS Catal. 2012, 2, 2795−2809

measure of the antipoisoning ability and stability of the catalyst: a longer time taken for the potential jump indicates higher antipoisoning ability and stability of the electrocatalyst; a lower polarization potential/overpotential before the potential jump shows higher activity of the electrocatalysts.[62]

From the chronopotentiometry profiles in Figure 13, it is seen that as compared with bare Pt/C sample, the CeO_2-modified Pt/C sample electrodes maintain a lower overpotential as well as much longer time for the potential jump, which unambiguously demonstrates the promoting activity of CeO_2 for a better antipoisoning ability and stability of the Pt/C electrocatalysts. In addition, under similar current density conditions, the methanol electrooxidation on the nanostructured shuttle-shaped, CeO_2-promoted Pt/C sample (Pt/CeO_2-HP/C) occurs at a lower overpotential, with a longer time (432 min) taken for the potential jump than the time taken (216 min) by the bulk CeO_2-promoted Pt/C sample (Pt/CeO_2-H/C). This clearly shows a remarkable improvement in the antipoisoning activity and long-time stability of Pt/C by the synergetic effect of the nanostructured shuttle-shaped CeO_2 as compared with bulk CeO_2 for methanol electrooxidation reaction. This is attributed to the smaller and uniform Pt nanoparticles and the formation of a higher concentration of oxygen-containing species (such as OH_{ads}) on the surface of shuttle-shaped CeO_2 at lower overpotential.

The steady state chronopotentiometry profile of the Pt/CeO_2-HP/C sample electrode clearly shows potential oscillations (Figure 13) at different time intervals. This is due to the formation and subsequent removal of carbonaceous species on the catalyst surface during the breakdown and dehydrogenation of methanol. Under constant current density polarization, methanol electrooxidation occurs at a particular potential, which is higher than the onset potential; however, the intermediate species, such as CO_{ads} and CHO_{ads}, on the catalyst surface make the oxidation overpotential shift to a higher value than the normal potential for methanol electrooxidation. At a certain high potential, the intermediate carbonaceous species get electrooxidized, and thereby, fresh Pt sites are generated for further adsorption and electrooxidation of methanol. At the electrooxidation overpotential of carbonaceous species, a sudden drop in the potential occurs, which shows generation of fresh Pt sites for subsequent reaction at a lower potential. After a certain time interval, the electrocatalyst again loses its activity due poisoning, and therefore, the potential keeps increasing until the water gets electrolyzed.[28,62]

The periodic electrooxidation of methanol and intermediate carbonaceous species results in potential oscillations during the steady-state process. Although the potential oscillation in the Pt/CeO_2-HP/C electrocatalyst indicates severe poisoning,[82] the polarization time for starting of this potential oscillation is significantly higher than the deactivation time for Pt/C as well as the bulk CeO_2-promoted Pt/C electrocatalysts. These results indicate that well-defined nanostructures of CeO_2 with a high surface area and uniform crystallographic surface provide enhanced antipoisoning activity and stability to the Pt/C electrocatalyst for the methanol electrooxidation reaction.

The superior electrochemical activity of CeO_2-promoted Pt/C samples was further investigated by chronoamperometry (steady state current at fixed potential) analysis, and the results are compared with a similar analysis on the Pt/C sample. The typical chronoamperometry profiles of Pt/C, Pt/CeO_2-H/C, and Pt/CeO_2-HP/C sample electrodes measured in 0.5 mol L^{-1} H_2SO_4 + 1 M CH_3OH solution at a fixed potential of 0.6 V (vs Ag/AgCl) for 7200 s are shown in Figure 14. The anodic potential of 0.6 V (vs Ag/AgCl), being closer to the methanol oxidation peak potential of the electrocatalysts, was chosen as the applied potential for the chronoamperometry measurements. From chronoamperometry responses of the three electrocatalysts, it is obvious that the CeO_2-modified Pt/C samples exhibit a higher oxidation current as well as lesser current decay with polarization time during the methanol electrooxidation reaction. For instance, the specific current responses of the Pt/C, Pt/CeO_2-H/C, and Pt/CeO_2-HP/C sample electrodes after 3600 s are 1.03, 2.58, and 5.59 mA cm^{-2}. The higher oxidation currents of CeO_2-promoted Pt/C samples as compared with the Pt/C sample once again demonstrate the promoting activity of CeO_2 for methanol electrooxidation,[24,26,27] which agrees well with the cyclic voltammetry and chronopotentiometry results.

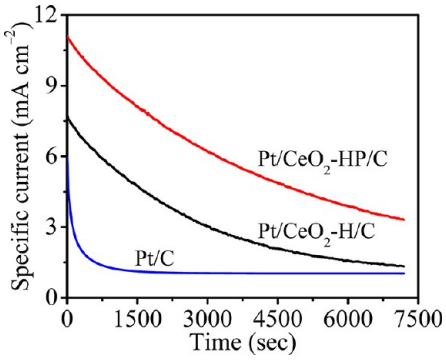

Figure 14. Chronoamperometric profiles of Pt/C, Pt/CeO_2-H/C, and Pt/CeO_2-HP/C sample electrodes in 0.5 mol L^{-1} H_2SO_4 + 1 M CH_3OH solution at 0.6 V.

Usually, sharp initial current drops occur for Pt/C electrocatalysts during the initial chronoamperometry scan for ~300 s, which is essentially due to the accretion of carbonaceous reaction intermediates such as CO and CHO on the active Pt surface sites and subsequent inhibition of MeOH adsorption as well as electrooxidation. However, the decrease in the specific current for the CeO_2-promoted samples with polarization time is rather gradual. These results clearly show the promoting activity of CeO_2 for resistance to catalyst poisoning by intermediate species during methanol electrooxidation. In addition, the current response of the shuttle-shaped, CeO_2-promoted Pt/C is significantly higher with a much slower decay with polarization time as compared with the bulk CeO_2-promoted Pt/C electrocatalyst.

In some recent reports, it is shown that, for direct Pt/CeO_2 interaction, there is a possibility of Pt crystallites invading into the CeO_2 lattice, which essentially deforms the surface structure of CeO_2.[36,77] However, in our study, the dispersion of Pt on the CeO_2 support is a triphasic situation in which Pt particles also share a larger part of their surfaces with conductive carbon. Therefore, the invasion of Pt particles directly into the CeO_2 lattice is expected to be minimal, and thus, deformation of the morphology and crystallographic identity of CeO_2 may also be insignificant. Regarding the solubility issue of CeO_2 in acids, it can be mentioned here that CeO_2 is insoluble in very mild acids, such as 0.5 M H_2SO_4 (used for this study), and hence, it is noncorrosive.[37] In fact, a recent report by Gu et al.,[37] suggests that the presence of CeO_2 essentially reduces the corrosion of XC-72 carbon black under continuous potential cycling in 0.5 M H_2SO_4 medium. Again, the strong interaction of CeO_2

dx.doi.org/10.1021/cs300473e | ACS Catal. 2012, 2, 2795−2809

with Pt can further reduce any small corrosion of CeO_2 in the Pt/CeO_2/C composite during the electrochemical studies.

The findings in this work demonstrate the nanostructure effect of oxide promoters to Pt/C for the methanol electrooxidation reaction, which is significant in the context of providing new insights for further development and designing of efficient electrocatalyst materials for DMFC applications.

4. CONCLUSIONS

In this work, we have demonstrated the microstructurization of CeO_2 by a shape-directing agent and synthesized uniquely structured CeO_2 (shuttle-shaped) at a large scale by employing a simple polymer (P123)-assisted homogeneous precipitation method under hydrothermal conditions. The physicochemical properties studied using PXRD, BET, and HRSEM techniques show a smaller crystallite size (~6.8 nm) and higher surface area (109 $m^2\ g^{-1}$) as well as pore volume (0.11 $cm^3\ g^{-1}$) and uniform shuttle-shaped surface morphology of the CeO_2 sample synthesized under the polymer-assisted method, as compared with the CeO_2 sample synthesized in the absence of a polymer, which shows a larger crystallite size (~12.3 nm) and lower surface area (80 $m^2\ g^{-1}$) as well as pore volume (0.08 $cm^3\ g^{-1}$) and undefined random platelike surface morphology. The H_2-TPR study shows very low temperature surface reduction of nanostructured shuttle-shaped CeO_2, which is due to the combined effect of the high surface area, smaller crystallite size, and larger size and number of surface oxygen vacancy clusters.

The HRTEM analysis of the Pt-loaded composites shows that shuttle-shaped CeO_2 promotes miniaturization and better dispersion of Pt crystallites. Cyclic voltammetry study shows a higher electroactive surface area of the shuttle-shaped CeO_2-promoted Pt/C sample compared with the bulk CeO_2-promoted Pt/C and bare Pt/C samples. In addition, the methanol oxidation activity using cyclic voltammetry and CO stripping voltammetry studies show a higher promoting effect (higher methanol and CO oxidation current density at lower overpotential) of nanostructured shuttle-shaped CeO_2, which is attributed to the large surface area, active surface crystalline facets, and large triple-phase interface area. The activity studies employing chronopotentiometry and chronoamperometry techniques illustrate that, unlike bulk CeO_2, nanostructured shuttle-shaped CeO_2 induces significant anti-CO poisoning activity to the Pt/C during methanol electrooxidation reaction. This is attributed to uniform active surface crystallites of nanostructured shuttle-shaped CeO_2, which provide higher number of labile OH_{ads} species for oxidation of carbonaceous species on the Pt surface at a lower overpotential. Overall, the present study details the characteristic surface modification of CeO_2 by a polymer and provides a rationale for the possible improvement in the electrocatalytic activity of Pt/C by suitable microstructures of CeO_2.

AUTHOR INFORMATION

Corresponding Author

*Phone: (+91) 44 2257 4226. Fax: (+91) 44 2257 0545. E-mail: grrao@iitm.ac.in.

Notes

The authors declare no competing financial interest.

ACKNOWLEDGMENTS

We acknowledge MNRE, New Delhi, for providing the CHI 7081C electrochemical workstation to carry out the electrochemical measurements and the SERC division of DST, Ministry of Science and Technology, New Delhi, for providing powder XRD, TGA, and BET facilities (under FIST Schemes).

REFERENCES

(1) Carrette, L.; Friedrich, K. A.; Stimming, U. *ChemPhysChem* **2001**, *1*, 162−193.
(2) Carrette, L.; Friedrich, K. A.; Stimming, U. *Fuel Cells* **2001**, *1*, 5−39.
(3) Stambouli, A. B. *Renewable Sustainable Energy Rev.* **2011**, *15*, 4507−4520.
(4) Hamnett, A. *Catal. Today* **1997**, *38*, 445−457.
(5) Wasmus, S.; Küver, A. *J. Electroanal. Chem.* **1999**, *461*, 14−31.
(6) Zhang, J.; Liu, H. *Electrocatalysis of Direct Methanol Fuel Cells*: Wiley-VCH: Weinheim, 2009.
(7) Yu, E. H.; Wang, X.; Krewer, U.; Li, L.; Scott, K. *Energy Environ. Sci* **2012**, *5*, 5668−5680.
(8) Cameron, D. S.; Hards, G. A.; Harrison, B.; Potter, R. J. *Platinum Met. Rev.* **1987**, *31*, 173−181.
(9) Shrestha, S.; Liu, Y.; Mustain, W. E. *Catal. Rev.: Sci. Eng.* **2011**, *53*, 256−336.
(10) García, G.; Koper, M. T. M. *ChemPhysChem* **2011**, *12*, 2064−2072.
(11) Rabis, A.; Rodriguez, P.; Schmidt, T. J. *ACS Catal.* **2012**, *2*, 864−890.
(12) Gurau, B.; Viswanathan, R.; Liu, R.; Lafrenz, T. J.; Ley, K. L.; Smotkin, E. S.; Reddington, E.; Sapienza, A.; Chan, B. C.; Mallouk, T. E. *J. Phys. Chem. B* **1998**, *102*, 9997−10003.
(13) Antolini, E.; Salgado, J. R. C.; Gonzalez, E. R. *J. Power Sources* **2006**, *160*, 957−968.
(14) Mukerjee, S.; Urian, R. C. *Electrochim. Acta* **2002**, *47*, 3219−3231.
(15) Cuesta, A. *ChemPhysChem* **2011**, *12*, 2375−2385.
(16) Qiao, Y.; Li, C. M. *J. Mater. Chem.* **2011**, *21*, 4027−4036.
(17) Antolini, E.; Perez, J. *J. Mater. Sci.* **2011**, *46*, 4435−4457.
(18) Yuan, H.; Guo, D.; Qiu, X.; Zhu, W.; Chen, L. *J. Power Sources* **2009**, *188*, 8−13.
(19) Ranga Rao, G.; Justin, P.; Meher, S. K. *Catal. Surv. Asia* **2011**, *15*, 221−229.
(20) Selvaganesh, S. V.; Selvarani, G.; Sridhar, P.; Pitchumani, S.; Shukla, A. K. *J. Electrochem. Soc.* **2012**, *159*, B463−B470.
(21) Jayaraman, S.; Jaramillo, T. F.; Baeck, S.-H.; McFarland, E. W. *J. Phys. Chem. B* **2005**, *109*, 22958−22966.
(22) Song, H.; Qiu, X.; Li, F. *Appl. Catal., A* **2009**, *364*, 1−7.
(23) Huang, T.; Zhuang, J.; Yu, A. *J. Appl. Electrochem.* **2009**, *39*, 1053−1058.
(24) Justin, P.; Ranga Rao, G. *Int. J. Hydrogen Energy* **2011**, *36*, 5875−5884.
(25) Tian, M.; Wu, G.; Chen, A. *ACS Catal.* **2012**, *2*, 425−432.
(26) Justin, P.; Ranga Rao, G. *Catal. Today* **2009**, *141*, 138−143.
(27) Justin, P.; Charan, P. H. K.; Ranga Rao, G. *Appl. Catal., B* **2010**, *100*, 510−515.
(28) Xu, C.; Shen, P. K. *Chem. Commun.* **2004**, 2238−2239.
(29) Campbell, C. T.; Peden, C. H. F. *Science* **2005**, *309*, 713−714.
(30) Campos, C. L.; Roldán, C.; Aponte, M.; Ishikawa, Y.; Cabrera, C. R. *J. Electroanal. Chem.* **2005**, *581*, 206−215.
(31) Wang, J.; Deng, X.; Xi, J.; Chen, L.; Zhu, W.; Qiu, X. *J. Power Sources* **2007**, *170*, 297−302.
(32) Takahashi, M.; Mori, T.; Ye, F.; Vinu, A.; Kobayashi, H.; Drennan, J. *J. Am. Ceram. Soc.* **2007**, *90*, 1291−1294.
(33) Scibioh, M. A.; Kim, S.-K.; Cho, E. A.; Lim, T.-H.; Hong, S.-A.; Ha, H. Y. *Appl. Catal., B* **2008**, *84*, 773−782.
(34) Zhou, Y.; Gao, Y.; Liu, Y.; Liu, J. *J. Power Sources* **2010**, *195*, 1605−1609.
(35) Chu, Y.-Y.; Wang, Z.-B.; Jiang, Z.-Z.; Gu, D.-M.; Yin, G.-P. *Adv. Mater.* **2011**, *23*, 3100−3104.
(36) Ou, D. R.; Mori, T.; Togasaki, H.; Takahashi, M.; Ye, F.; Drennan, J. *Langmuir* **2011**, *27*, 3859−3866.

(37) Gu, D.-M.; Chu, Y.-Y.; Wang, Z.-B.; Jiang, Z.-Z.; Yin, G.-P.; Liu, Y. *Appl. Catal., B* **2011**, *102*, 9−18.
(38) Meher, S. K.; Ranga Rao, G. *J. Colloid Interface Sci.* **2012**, *373*, 46−56.
(39) Liu, X.; Zhou, K.; Wang, L.; Wang, B.; Li, Y. *J. Am. Chem. Soc.* **2009**, *131*, 3140−3141.
(40) Farmer, J. A.; Campbell, C. T. *Science* **2010**, *329*, 933−936.
(41) Nagai, Y.; Hirabayashi, T.; Dohmae, K.; Takagi, N.; Minami, T.; Shinjoh, H.; Matsumoto, S. *J. Catal.* **2006**, *242*, 103−109.
(42) Vayssilov, G. N.; Lykhach, Y.; Migani, A.; Staudt, T.; Petrova, G. P.; Tsud, N.; Skála, T.; Bruix, A.; Illas, F.; Prince, K. C.; Matolín, V.; Neyman, K. M.; Libuda, J. *Nat. Mater.* **2011**, *10*, 310−315.
(43) Yuan, Q.; Duan, H.-H.; Li, L.-L.; Sun, L.-D.; Zhang, Y.-W.; Yan, C.-H. *J. Colloid Interface Sci.* **2009**, *335*, 151−167.
(44) Orilall, M. C.; Wiesner, U. *Chem. Soc. Rev.* **2011**, *40*, 520−535.
(45) Jun, Y.; Choi, J.; Cheon, J. *Angew. Chem., Int. Ed.* **2006**, *45*, 3414−3439.
(46) Song, R.-Q.; Cölfen, H. *CrystEngComm* **2011**, *13*, 1249−1276.
(47) Gebauer, D.; Cölfen, H. *Nano Today* **2011**, *6*, 564−584.
(48) Mallavajula, R. K.; Archer, L. A. *Angew. Chem., Int. Ed.* **2011**, *50*, 578−580.
(49) Meher, S. K.; Justin, P.; Ranga Rao, G. *Nanoscale* **2011**, *3*, 683−692.
(50) Aneggi, E.; Boaro, M.; de Leitenburg, C.; Dolcetti, G.; Trovarelli, A. *J. Alloys Compd.* **2006**, *408*−*412*, 1096−1102.
(51) Ranga Rao, G. *Bull. Mater. Sci.* **1999**, *22*, 89−94.
(52) Migani, A.; Vayssilov, G. N.; Bromley, S. T.; Illas, F.; Neyman, K. M. *J. Mater. Chem.* **2010**, *20*, 10535−10546.
(53) Zhou, K.; Yang, Z.; Yang, S. *Chem. Mater.* **2007**, *19*, 1215−1217.
(54) Nolan, M.; Fearon, J. E.; Watson, G. W. *Solid State Ionics* **2006**, *177*, 3069−3074.
(55) Lu, Z.; Yang, Z. *J. Phys.: Condens. Matter* **2010**, *22*, 475003 (1−10).
(56) Yang, Z.; Lu, Z.; Luo, G. *Phys. Rev. B* **2007**, *76*, 075421-1−075421-10.
(57) Anumol, E. A.; Kundu, P.; Deshpande, P. A.; Madras, G.; Ravishankar, N. *ACS Nano* **2011**, *5*, 8049−8061.
(58) Huang, Y.; Huang, H.; Liu, Y.; Xie, Y.; Liang, Z.; Liu, C. *J. Power Sources* **2012**, *201*, 81−87.
(59) Feng, L.; Hoang, D. T.; Tsung, C.-K.; Huang, W.; Lo, S. H.-Y.; Wood, J. B.; Wang, H.; Tang, J.; Yang, P. *Nano Res.* **2011**, *4* (1), 61−71.
(60) Mullins, D. R.; Overbury, S. H.; Huntley, D. R. *Surf. Sci.* **1998**, *409*, 307−319.
(61) Sun, Z.; Zhang, H.; An, G.; Yang, G.; Liu, Z. *J. Mater. Chem.* **2010**, *20*, 1947−1952.
(62) Buck, R. P.; Griffith, L. R. *J. Electrochem. Soc.* **1962**, *109*, 1005−1013.
(63) Hu, C.-C.; Liu, K.-Y. *Electrochim. Acta* **1999**, *44*, 2727−2738.
(64) Zolfaghari, A.; Chayer, M.; Jerkiewicz, G. *J. Electrochem. Soc.* **1997**, *144*, 3034−3041.
(65) Chen, Q.-S.; Vidal-Iglesias, F. J.; Solla-Gullón, J.; Sun, S.-G.; Feliu, J. M. *Chem. Sci.* **2012**, *3*, 136−147.
(66) Solla-Gullón, J.; Rodríguez, P.; Herrero, E.; Aldaz, A.; Feliu, J. M. *Phys. Chem. Chem. Phys.* **2008**, *10*, 1359−1373.
(67) Sheng, W.; Gasteiger, H. A.; Shao-Horn, Y. *J. Electrochem. Soc.* **2010**, *157*, B1529−B1536.
(68) Umeda, M.; Kokubo, M.; Mohamedi, M.; Uchida, I. *Electrochim. Acta* **2003**, *48*, 1367−1374.
(69) Zeng, J. *J. Mater. Chem.* **2012**, *22*, 3170−3176.
(70) Schmidt, J.; Gasteiger, H. A.; Stab, G. D.; Urban, P. M.; KoIb, D. M.; Behm, R. J. *J. Electrochem. Soc.* **1998**, *145*, 2354−2358.
(71) Pozio, A.; De Francesco, M.; Cemmi, A.; Cardellini, F.; Giorgi, L. *J. Power Sources* **2002**, *105*, 13−19.
(72) Solla-Gullón, J.; Vidal-Iglesias, F. J.; Feliu, J. M. *Annu. Rep. Prog. Chem., Sect. C: Phys. Chem.* **2011**, *107*, 263−297.
(73) Iwasita, T. *Electrochim. Acta* **2002**, *47*, 3663−3674.
(74) Hofstead-Duffy, A. M.; Chen, D.-J.; Sun, S.-G.; Tong, Y. Y. J. *J. Mater. Chem.* **2012**, *22*, 5205−5208.
(75) López-Cudero, A.; Cuesta, A.; Gutiérrez, C. *J. Electroanal. Chem.* **2006**, *586*, 204−216.
(76) O'Hayre, R.; Barnett, D. M.; Prinz, F. B. *J. Electrochem. Soc.* **2005**, *152*, A439−A444.
(77) Ou, D. R.; Mori, T.; Fugane, K.; Togasaki, H.; Ye, F.; Drennan, J. *J. Phys. Chem. C* **2011**, *115*, 19239−19245.
(78) Krewer, U.; Vidakovic-Koch, T.; Rihko-Struckmann, L. *ChemPhysChem* **2011**, *12*, 2518−2544.
(79) Ochal, P.; Fuente, J. L. G.; Tsypkin, M.; Seland, F.; Sunde, S.; Muthuswamy, N.; Ronning, M.; Chen, D.; Garcia, S.; Alayoglu, S.; Eichhorn, B. *J. Electroanal. Chem.* **2011**, *655*, 140−146.
(80) Susut, C.; Chapman, G. B.; Samjeské, G.; Osawac, M.; Tong, Y. Y. *Phys. Chem. Chem. Phys.* **2008**, *10*, 3712−3721.
(81) Evarts, S. E.; Kendrick, I.; Wallstrom, B. L.; Mion, T.; Abedi, M.; Dimakis, N.; Smotkin, E. S. *ACS Catal.* **2012**, *2*, 701−707.
(82) Hu, F.; Chen, C.; Wang, Z.; Wei, G.; Shen, P. K. *Electrochim. Acta* **2006**, *52*, 1087−1091.